



Linear response calculation with nonlocal van der Waals density functionalsKazutoshi Miwa ^{*}*Toyota Central Research & Development Laboratories, Inc., Nagakute, Aichi 480-1192, Japan* (Received 31 October 2021; revised 29 December 2021; accepted 10 January 2022; published 24 January 2022)

The linear-response approach with the nonlocal van der Waals density functionals is presented, considering three kinds of perturbations: Atomic displacements, uniform electric fields, and strain. The formulas to compute the response with respect to strain are derived for the van der Waals density functionals as well as for the generalized gradient approximation. The linear-response method is implemented within the ultrasoft pseudopotential scheme. The method is applied to weak-coupled layered materials, graphite and MoS₂. The results support the validity of the derived formulas and demonstrate the utilities of the linear-response method for weak-coupled van der Waals systems.

DOI: [10.1103/PhysRevB.105.024109](https://doi.org/10.1103/PhysRevB.105.024109)**I. INTRODUCTION**

Long-range van der Waals (vdW) forces play an important role for sparse systems such as molecular solids, weak-coupled layered materials, surface physisorption, and so on. The local density approximation (LDA) [1–3] and semilocal generalized gradient approximation (GGA) [4–6], which are commonly adopted for the exchange-correlation (XC) functional in density functional theory (DFT) calculations, cannot describe this interaction properly [7]. To deal with the long-range vdW interaction within DFT, nonlocal density functionals have been proposed [8–10] and successfully applied to sparse systems [11]. An efficient interpolation formula for a double spatial integral of the nonlocal functionals has been also presented [12,13], which provides remarkable reduction of the computational cost.

In DFT calculations, the total energy is the most fundamental quantity and the derivatives of it are closely related to various properties of a material. A simple way to compute the second derivatives of the total energy is a finite-difference (FD) approach in which they are computed from numerical differentiation of the first derivatives by applying small perturbations to a system. Alternatively, the linear-response (LNR) methods [14–21] have been developed to compute them in an accurate and efficient manner. The LNR approach has several advantages over the FD method. The uniform electric field, which does not satisfy a periodic boundary condition, can be treated by taking a long-wavelength limit analytically [15,22,23]. The phonons with finite wave vectors can be calculated with the unit cell using the phase factorization approach [15]. When the LNR calculations are completed, one can access total-energy derivatives up to the third order such as phonon anharmonic couplings [24] and Raman susceptibility tensors [23]. The phonon calculation using the LNR method has already been extended to treat the vdW density functionals [25].

In this paper, I report the LNR method with the vdW density functionals considering three kinds of perturbations:

Atomic displacements, uniform electric fields, and strain. For the strain perturbation, the previous studies [26,27] support only the LDA functionals. Thus, the expressions to compute the response with respect to strain are derived for the vdW density functionals as well as the GGA functionals. Since van der Waals solids are generally very soft, one must pay attention to numerical precision of stresses and atomic forces when the elastic constant tensor is calculated using the FD method. The LNR method enables an accurate and efficient treatment of soft materials due to direct evaluation of the response to strain. The present LNR method is implemented within the ultrasoft pseudopotential scheme [23,28–30].

The rest of this paper is organized as follows: The formulas to compute the response to external perturbations are presented in Sec. II. In Sec. III, the method is applied to graphite and molybdenum disulfide (MoS₂). Section IV gives a summary of this study.

II. METHODOLOGY**A. Linear-response method**

When an external perturbation λ is imposed on a system, the first-order change of the Kohn-Sham Hamiltonian $\frac{dH}{d\lambda}$ is induced. This causes the first-order change in the wave function $\frac{d\Psi_n}{d\lambda}$ and then in the charge density $\frac{d\rho}{d\lambda}$. In the LNR method, these three quantities are computed by self-consistently solving the Sternheimer equation [31,32]. The mixed second derivative of the total energy respect to two perturbations can be calculated from the nonstationary expression [16] if the response to one of the two perturbations is available. To compute the mixed third derivative of the total energy, all the related responses are required.

The DFT code used in this study has been developed by the author. The LNR calculations with this code have already been applied to various systems [23,29,30,33,34]. In this paper, I focus on the linear response of the exchange-correlation functionals. Detailed formulation of the other parts can be found in the published LNR papers. I refer to Ref. [35] for the phonon calculation, Ref. [23] for the electric-field perturbation and the Raman susceptibility calculation, Ref. [27] for the

^{*}miwa@cmp.tytlabs.co.jp

strain perturbation, and Ref. [17] for the treatment of metallic systems.

B. van der Waals density functional

Hereafter, I use the charge density ρ for the sum of the valence charge density ρ_v and the partial core charge density ρ_c [36]. The nonlocal correlation functional proposed by Dion *et al.* [8] has the following form:

$$E_c^{\text{vdW}}[\rho] = \frac{1}{2} \iint \rho(\mathbf{r})\phi(q(\mathbf{r}), q(\mathbf{r}'), |\mathbf{r} - \mathbf{r}'|)\rho(\mathbf{r}') d\mathbf{r}d\mathbf{r}', \quad (1)$$

where ϕ is a nonlocal kernel, and $q = q(\rho(\mathbf{r}), g(\mathbf{r}))$ is a universal function that depends on the charge density ρ and its gradient $g = |\nabla\rho|$. This nonlocal functional is combined with the GGA exchange functional E_x^{GGA} and the LDA correlation functional E_c^{LDA} to form the van der Waals density functional for the XC energy,

$$E_{xc}[\rho, g] = E_x^{\text{GGA}}[\rho, g] + E_c^{\text{LDA}}[\rho] + E_c^{\text{vdW}}[\rho, g]. \quad (2)$$

The double spatial integral of Eq. (1) requires considerable computational effort. Román-Pérez and Soler [12] proposed an efficient algorithm to evaluate it. A modified version was also proposed by Wu and Gygi [13]. In their approaches, the q function is discretized to N_q points, q_n ($n = 1, \dots, N_q$), and the kernel ϕ is computed on a two-dimensional grid of fixed q values in advance. Then, the values of ϕ at \mathbf{r} and \mathbf{r}' are interpolated using a bilinear combination of the cubic splines $p_n(q)$. In this study, the Wu-Gygi implementation is adopted,

which is free from a logarithmic singularity of ϕ at $q(\mathbf{r}) = q(\mathbf{r}') = 0$. Equation (1) is rewritten as

$$E_c^{\text{vdW}} = \frac{1}{2} \sum_{mn} \iint \theta_m(\mathbf{r})\Phi_{mn}(|\mathbf{r} - \mathbf{r}'|)\theta_n(\mathbf{r}') d\mathbf{r}d\mathbf{r}', \quad (3)$$

where

$$\theta_n(\mathbf{r}) = \frac{\rho(\mathbf{r})p_n(q(\mathbf{r}))}{q(\mathbf{r})}, \quad (4)$$

and

$$\Phi_{mn}(r) = q_m q_n \phi(q_m, q_n, r). \quad (5)$$

Since the q functions in Φ_{mn} are fixed independent of \mathbf{r} and \mathbf{r}' , the integral of Eq. (3) becomes a simple convolution that can be calculated efficiently using the fast Fourier transform.

Applying the discretized technique proposed by White and Bird [37], the correlation potential associated with E_c^{vdW} is obtained as

$$V_c^{\text{vdW}}(\mathbf{r}) = \sum_n \left(u_n \frac{\partial \theta_n}{\partial \rho} - \sum_{\xi} \nabla_{\xi} u_n \frac{\partial \theta_n}{\partial g} \frac{g_{\xi}}{g} \right), \quad (6)$$

where $g_{\xi} = \nabla_{\xi} \rho$ and

$$u_n(\mathbf{r}) = \sum_n \int \Phi_{mn}(|\mathbf{r} - \mathbf{r}'|)\theta_n(\mathbf{r}') d\mathbf{r}'. \quad (7)$$

The discretized formula was also extended to the first derivative of the XC potential in the LNR calculation [38]. Applying it, the first derivative of V_c^{vdW} with respect to an external perturbation λ is expressed as

$$\begin{aligned} \frac{dV_c^{\text{vdW}}(\mathbf{r})}{d\lambda} &= \int \frac{\delta^2 E_c^{\text{vdW}}}{\delta \rho(\mathbf{r}) \delta \rho(\mathbf{r}')} \frac{d\rho(\mathbf{r}')}{d\lambda} d\mathbf{r}' \\ &= \sum_n \left(u_n \frac{\partial^2 \theta_n}{\partial \rho^2} \frac{d\rho}{d\lambda} + \sum_{\xi} u_n \frac{\partial^2 \theta_n}{\partial \rho \partial g} \frac{g_{\xi}}{g} \nabla_{\xi} \frac{d\rho}{d\lambda} - \sum_{\xi'} \nabla_{\xi'} \left\{ u_n \frac{\partial^2 \theta_n}{\partial \rho \partial g} \frac{g_{\xi'}}{g} \frac{d\rho}{d\lambda} \right. \right. \\ &\quad \left. \left. + \sum_{\xi} u_n \left(\frac{\partial^2 \theta_n}{\partial g^2} \frac{g_{\xi'} g_{\xi}}{g^2} + \frac{\partial \theta_n}{\partial g} \left(\frac{\delta_{\xi' \xi}}{g} - \frac{g_{\xi'} g_{\xi}}{g^3} \right) \right) \nabla_{\xi} \frac{d\rho}{d\lambda} \right\} + \frac{\partial \theta_n}{\partial \rho} t_n^{\lambda} - \sum_{\xi} \nabla_{\xi} \frac{\partial \theta_n}{\partial g} \frac{g_{\xi}}{g} t_n^{\lambda} \right), \quad (8) \end{aligned}$$

where $\frac{d\rho}{d\lambda}$ is the first-order charge density and

$$t_m^{\lambda}(\mathbf{r}) = \sum_n \int \Phi_{mn}(|\mathbf{r} - \mathbf{r}'|) \left(\frac{\partial \theta_n(\mathbf{r}')}{\partial \rho} \frac{d\rho(\mathbf{r}')}{d\lambda} + \sum_{\xi} \frac{\partial \theta_n(\mathbf{r}')}{\partial g} \frac{g_{\xi}(\mathbf{r}')}{g(\mathbf{r}')} \nabla_{\xi} \frac{d\rho(\mathbf{r}')}{d\lambda} \right) d\mathbf{r}'. \quad (9)$$

Equation (8) can be used for atomic-displacement and electric-field perturbations. In the phonon calculations with incommensurate wave vectors \mathbf{q} , the phase factorization approach [15] is utilized. In these cases, the spatial gradient operators in Eqs. (8) and (9) should be changed as $\nabla_{\xi} \rightarrow \iota q_{\xi} + \nabla_{\xi}$.

The Raman susceptibility calculation is straightforward if the LNR calculations with respect to the atomic-displacement and electric-field perturbations are completed. The Raman susceptibility tensor is closely related to the mixed third derivative of the total energy with respect to a uniform electric field twice and an atomic displacement. To compute it, the

third-order change of the correlation energy is required. The third-order correlation energy can be obtained by numerically differentiating the second-order correlation energy of Eq. (8) as shown in Ref. [23].

C. Elastic constant tensor

The elastic constant tensor and related quantities can be obtained from the LNR calculations with respect to strain perturbations. If the XC functional depends on the density gradient such as the GGA and vdW functionals, additional terms have to be taken into account.

First, the GGA functionals are considered since Eq. (2) includes the GGA exchange functional. For a given GGA kernel f , the XC energy and potential are represented as $E_{xc}^{GGA} = \int f(\rho(\mathbf{r}), g(\mathbf{r})) d\mathbf{r}$ and $V_{xc}^{GGA} = \frac{\partial f}{\partial \rho} - \sum_{\xi} \nabla_{\xi} \frac{\partial f}{\partial g} \frac{g_{\xi}}{g}$, respectively. The XC contribution to the stress tensor is given by [39,40]

$$\frac{\partial E_{xc}^{GGA}}{\partial \epsilon_{\alpha\beta}} = \delta_{\alpha\beta} E_{xc}^{GGA} + \int V_{xc}^{GGA} \frac{\partial \rho}{\partial \epsilon_{\alpha\beta}} d\mathbf{r} - \int \frac{\partial f}{\partial g} \frac{g_{\alpha} g_{\beta}}{g} d\mathbf{r}, \quad (10)$$

where $\epsilon_{\alpha\beta}$ is the strain tensor and $\frac{\partial \rho}{\partial \epsilon_{\alpha\beta}} = -\delta_{\alpha\beta} \rho_v + \frac{\partial \rho_c}{\partial \epsilon_{\alpha\beta}}$. The first two terms in the right-hand side of Eq. (10) are LDA-like

ones [41]. The third term comes from the fact that the strain scales the gradient as $\nabla_{\alpha} \rightarrow (\delta_{\beta\alpha} - \epsilon_{\beta\alpha}) \nabla_{\beta}$. Similarly, additional terms due to gradient scaling should be considered for the first derivative of the XC potential in the LNR calculation,

$$\frac{dV_{xc}^{GGA}(\mathbf{r})}{d\epsilon_{\alpha\beta}} = \int \frac{\delta^2 E_{xc}^{GGA}}{\delta \rho(\mathbf{r}) \delta \rho(\mathbf{r}')} \frac{d\rho(\mathbf{r}')}{d\epsilon_{\alpha\beta}} d\mathbf{r}' + F_{\alpha\beta}^{GGA}(\mathbf{r}), \quad (11)$$

where the first term is an LDA-like one [26,27] and the second term contains the gradient-scaling contribution,

$$F_{\alpha\beta}^{GGA} = -\frac{\partial^2 f}{\partial \rho \partial g} \frac{g_{\alpha} g_{\beta}}{g} + \sum_{\xi} \nabla_{\xi} \left(\frac{\partial^2 f}{\partial g^2} \frac{g_{\xi} g_{\alpha} g_{\beta}}{g^2} + \frac{\partial f}{\partial g} \left(\delta_{\xi\alpha} \frac{g_{\beta}}{g} + \delta_{\xi\beta} \frac{g_{\alpha}}{g} - \frac{g_{\xi} g_{\alpha} g_{\beta}}{g^3} \right) \right). \quad (12)$$

Because the gradient-scaling function $F_{\alpha\beta}^{GGA}$ does not depend on $\frac{d\rho}{d\epsilon_{\alpha\beta}}$, the self-consistent-field (SCF) treatment is unnecessary for it. The mixed second derivative of the XC energy with respect to two strain perturbations is also affected by gradient-scaling terms,

$$\begin{aligned} \frac{\partial^2 E_{xc}^{GGA}}{\partial \epsilon_{\alpha\beta} \partial \epsilon_{\gamma\eta}} &= \delta_{\alpha\beta} \delta_{\gamma\eta} E_{xc}^{GGA} + \int V_{xc}^{GGA} \left(\delta_{\gamma\eta} \frac{\partial \rho}{\partial \epsilon_{\alpha\beta}} + \delta_{\alpha\beta} \frac{\partial \rho}{\partial \epsilon_{\gamma\eta}} + \frac{\partial^2 \rho}{\partial \epsilon_{\alpha\beta} \partial \epsilon_{\gamma\eta}} \right) d\mathbf{r} + \iint \frac{\delta^2 E_{xc}^{GGA}}{\delta \rho(\mathbf{r}) \delta \rho(\mathbf{r}')} \frac{\partial \rho}{\partial \epsilon_{\alpha\beta}} \frac{\partial \rho}{\partial \epsilon_{\gamma\eta}} d\mathbf{r} d\mathbf{r}' \\ &+ \int \left(F_{\alpha\beta}^{GGA} \frac{\partial \rho}{\partial \epsilon_{\gamma\eta}} + F_{\gamma\eta}^{GGA} \frac{\partial \rho}{\partial \epsilon_{\alpha\beta}} \right) d\mathbf{r} + \int \left(\frac{\partial^2 f}{\partial g^2} \frac{g_{\alpha} g_{\beta} g_{\gamma} g_{\eta}}{g^2} - \frac{\partial f}{\partial g} \left(\delta_{\alpha\beta} \frac{g_{\gamma} g_{\eta}}{g} + \delta_{\gamma\eta} \frac{g_{\alpha} g_{\beta}}{g} + \frac{g_{\alpha} g_{\beta} g_{\gamma} g_{\eta}}{g^3} \right. \right. \\ &\left. \left. - \frac{\delta_{\alpha\gamma} g_{\eta} g_{\beta} + \delta_{\alpha\eta} g_{\gamma} g_{\beta} + \delta_{\beta\gamma} g_{\alpha} g_{\eta} + \delta_{\beta\eta} g_{\alpha} g_{\gamma}}{2g} \right) \right) d\mathbf{r}. \end{aligned} \quad (13)$$

This second derivative corresponds to the clamped-ion elastic constant that is independent of the atomic relaxation caused by lattice deformation. The force-strain coupling tensor is required to calculate the physically relevant relaxed-ion elastic constant [42]. The XC contribution to this coupling tensor also includes the gradient-scaling function,

$$\frac{\partial^2 E_{xc}^{GGA}}{\partial \epsilon_{\alpha\beta} \partial R_{I\gamma}} = \int V_{xc}^{GGA} \left(\delta_{\alpha\beta} \frac{\partial \rho_c}{\partial R_{I\gamma}} + \frac{\partial^2 \rho_c}{\partial \epsilon_{\alpha\beta} \partial R_{I\gamma}} \right) d\mathbf{r} + \iint \frac{\delta^2 E_{xc}^{GGA}}{\delta \rho(\mathbf{r}) \delta \rho(\mathbf{r}')} \frac{\partial \rho}{\partial \epsilon_{\alpha\beta}} \frac{\partial \rho_c}{\partial R_{I\gamma}} d\mathbf{r} d\mathbf{r}' + \int F_{\alpha\beta}^{GGA} \frac{\partial \rho_c}{\partial R_{I\gamma}} d\mathbf{r}, \quad (14)$$

where $R_{I\gamma}$ denotes the γ component of the I th atom position.

In the case of the vdW density functionals, the following gradient-scaling function should be added to Eq. (8) to construct the first derivative of V_c^{vdW} with respect to strain,

$$\begin{aligned} F_{\alpha\beta}^{vdW}(\mathbf{r}) &= \sum_n \left(-u_n \frac{\partial^2 \theta_n}{\partial \rho \partial g} \frac{g_{\alpha} g_{\beta}}{g} + \sum_{\xi} \nabla_{\xi} u_n \left\{ \frac{\partial^2 \theta_n}{\partial g^2} \frac{g_{\xi} g_{\alpha} g_{\beta}}{g^2} + \frac{\partial \theta_n}{\partial g} \left(\delta_{\xi\alpha} \frac{g_{\beta}}{g} + \delta_{\xi\beta} \frac{g_{\alpha}}{g} - \frac{g_{\xi} g_{\alpha} g_{\beta}}{g^3} \right) \right\} \right) \\ &+ (v_n^{\alpha\beta} + w_n^{\alpha\beta}) \frac{\partial \theta_n}{\partial \rho} - \sum_{\xi} \nabla_{\xi} (v_n^{\alpha\beta} + w_n^{\alpha\beta}) \frac{\partial \theta_n}{\partial g} \frac{g_{\xi}}{g}, \end{aligned} \quad (15)$$

where

$$v_m^{\alpha\beta}(\mathbf{r}) = -\sum_n \int \Phi_{mn}(|\mathbf{r} - \mathbf{r}'|) \frac{\partial \theta_n(\mathbf{r}')}{\partial g} \frac{g_{\alpha}(\mathbf{r}') g_{\beta}(\mathbf{r}')}{g(\mathbf{r}')} d\mathbf{r}', \quad (16)$$

and

$$w_m^{\alpha\beta}(\mathbf{r}) = \sum_n \int \frac{\partial \Phi_{mn}(|\mathbf{r} - \mathbf{r}'|)}{\partial \epsilon_{\alpha\beta}} \theta_n(\mathbf{r}') d\mathbf{r}'. \quad (17)$$

The contribution of E_c^{vdW} to the clamped-ion elastic constant is given by

$$\begin{aligned} \frac{\partial^2 E_c^{vdW}}{\partial \epsilon_{\alpha\beta} \partial \epsilon_{\gamma\eta}} &= \delta_{\alpha\beta} \delta_{\gamma\eta} E_c^{vdW} + \int V_c^{vdW} \left(\delta_{\gamma\eta} \frac{\partial \rho}{\partial \epsilon_{\alpha\beta}} + \delta_{\alpha\beta} \frac{\partial \rho}{\partial \epsilon_{\gamma\eta}} + \frac{\partial^2 \rho}{\partial \epsilon_{\alpha\beta} \partial \epsilon_{\gamma\eta}} \right) d\mathbf{r} + \iint \frac{\delta^2 E_c^{vdW}}{\delta \rho(\mathbf{r}) \delta \rho(\mathbf{r}')} \frac{\partial \rho}{\partial \epsilon_{\alpha\beta}} \frac{\partial \rho}{\partial \epsilon_{\gamma\eta}} d\mathbf{r} d\mathbf{r}' \\ &+ \int \left(F_{\alpha\beta}^{vdW} \frac{\partial \rho}{\partial \epsilon_{\gamma\eta}} + F_{\gamma\eta}^{vdW} \frac{\partial \rho}{\partial \epsilon_{\alpha\beta}} \right) d\mathbf{r} + \sum_n \int u_n \left(\frac{\partial^2 \theta_n}{\partial g^2} \frac{g_{\alpha} g_{\beta} g_{\gamma} g_{\eta}}{g^2} - \frac{\partial \theta_n}{\partial g} \left(\delta_{\alpha\beta} \frac{g_{\gamma} g_{\eta}}{g} + \delta_{\gamma\eta} \frac{g_{\alpha} g_{\beta}}{g} + \frac{g_{\alpha} g_{\beta} g_{\gamma} g_{\eta}}{g^3} \right. \right. \end{aligned}$$

$$\begin{aligned}
& - \frac{\delta_{\alpha\gamma}g_{\eta}g_{\beta} + \delta_{\alpha\eta}g_{\gamma}g_{\beta} + \delta_{\beta\gamma}g_{\alpha}g_{\eta} + \delta_{\beta\eta}g_{\alpha}g_{\gamma}}{2g} \Big) d\mathbf{r} + \sum_n \int \left(v_n^{\alpha\beta} \frac{\partial\theta_n}{\partial g} \frac{g_{\gamma}g_{\eta}}{g} + w_n^{\alpha\beta} \frac{\partial\theta_n}{\partial g} \frac{g_{\gamma}g_{\eta}}{g} + u_n^{\gamma\eta} \frac{\partial\theta_n}{\partial g} \frac{g_{\alpha}g_{\beta}}{g} \right) d\mathbf{r} \\
& + \frac{1}{2} \sum_{mn} \iint \theta_m \left(\delta_{\alpha\beta} \frac{\partial\Phi_{mn}}{\partial\epsilon_{\gamma\eta}} + \delta_{\gamma\eta} \frac{\partial\Phi_{mn}}{\partial\epsilon_{\alpha\beta}} + \frac{\partial^2\Phi_{mn}}{\partial\epsilon_{\alpha\beta}\partial\epsilon_{\gamma\eta}} \right) \theta_n d\mathbf{r}d\mathbf{r}'. \quad (18)
\end{aligned}$$

The contribution of E_c^{vdW} to the force-strain coupling tensor is expressed by the same form as in the case of GGA,

$$\frac{\partial^2 E_c^{\text{vdW}}}{\partial\epsilon_{\alpha\beta}\partial R_{I\gamma}} = \int V_c^{\text{vdW}} \left(\delta_{\alpha\beta} \frac{\partial\rho_c}{\partial R_{I\gamma}} + \frac{\partial^2\rho_c}{\partial\epsilon_{\alpha\beta}\partial R_{I\gamma}} \right) d\mathbf{r} + \iint \frac{\delta^2 E_c^{\text{vdW}}}{\delta\rho(\mathbf{r})\delta\rho(\mathbf{r}')} \frac{\partial\rho}{\partial\epsilon_{\alpha\beta}} \frac{\partial\rho_c}{\partial R_{I\gamma}} d\mathbf{r}d\mathbf{r}' + \int F_{\alpha\beta}^{\text{vdW}} \frac{\partial\rho_c}{\partial R_{I\gamma}} d\mathbf{r}. \quad (19)$$

D. Computational details

The optB86b-vdW functional [43] is adopted in this paper. As shown in Ref. [43], this functional gives accurate results not only for weak-coupled van der Waals systems, but also for traditional hard materials. A logarithmic mesh is used to discretize the q function, where $q_{n+1} - q_n = \lambda(q_n - q_{n-1})$ with $\lambda = 1.3$ and $q_0 = 0$. The number of mesh points and the maximum value of q are set to be $N_q = 20$ and $q_{N_q} = 5$ a.u., respectively. According to Ref. [12], the saturation function is introduced to the q function in order to prevent unfavorable extrapolation and stabilize the SCF calculation,

$$q^{\text{sat}}(\mathbf{r}) = q_{N_q} \left[1 - \exp\left(-\sum_{m=1}^{12} \frac{(q(\mathbf{r})/q_{N_q})^m}{m}\right) \right]. \quad (20)$$

When the finite strain is applied to a system, the number of the plane waves usually varies. It may cause an abrupt change in the total energy if a sufficiently large number of the plane waves is not used. A practical way to prevent this change with a moderate number of the plane waves is to add the smearing function to the kinetic-energy operator [44]. This treatment is necessary in the cell optimization to regularize the total-energy changes. In this paper, unless otherwise noted, the kinetic-energy smearing function is kept in the LNR calculations so as the residual stresses are consistent with the values determined in the optimization process.

The pseudopotentials constructed with the GGA-PBE functional [5] are used in this paper. It has been reported that the use of the GGA pseudopotentials in the calculations with the vdW density functional gives only a minor effect [45].

III. RESULTS AND DISCUSSION

A. Graphite

Graphite is a typical layered material with the vdW interaction. In this section, I mainly show the comparison between the LNR and FD calculations. The cutoff energies are set to be 15 and 160 hartrees for the wave function and charge density, respectively. A Γ -centered $16 \times 16 \times 8$ k -point mesh is used for the Brillouin zone integration and Gaussian smearing with a width of 6 mhartrees is applied.

Graphite has hexagonal symmetry with space group $P6_3/mmc$ (No. 194). The unit cell contains four C atoms located at $2b(0, 0, 1/4)$ and $2c(1/3, 2/3, 1/4)$ sites. The theoretical lattice constants calculated with the optB86b-vdW functional are $a = 2.478$ Å and $c = 6.680$ Å, which are in good agreement with the experimental data, $a = 2.462$ Å and

$c = 6.707$ Å [46]. The optB86b-vdW functional describes two quite different cohesive natures properly, strong covalent bonding between in-plane C atoms and weak vdW interaction between different layers.

The phonon dispersion of graphite is calculated by the LNR method. The dynamical matrices are calculated on a Γ -centered $8 \times 8 \times 4$ q -point mesh and the phonon frequencies along the high-symmetry lines of the Brillouin zone are obtained using the Fourier interpolation [16]. The frozen phonon calculations are also carried out using the $4 \times 4 \times 2$ supercell, in which the atomic displacements of ± 0.01 Å are applied for numerical differentiation. The results are shown in Fig. 1. The phonon frequencies obtained by the two methods are in good agreement within a mean absolute error of 0.6 cm^{-1} . The phonon dispersion curves calculated by the LNR method agree well with those of the previous calculation using the vdW density functionals [25].

The elastic constants are calculated by the LNR method and compared with the FD results. In the FD calculations, the strains of $\epsilon = \pm 5 \times 10^{-3}$ are applied. The clamped-ion and relaxed-ion constants are given in Table I, where Voigt notation is used. The agreement between the values computed by the two methods is fairly good. The differences between them are less than 1 GPa except for C_{11} and C_{12} for which the errors of about 2 GPa are found. The calculated relaxed-ion constants reasonably agree with the experimental data. Table II gives the force-strain coupling constants calculated

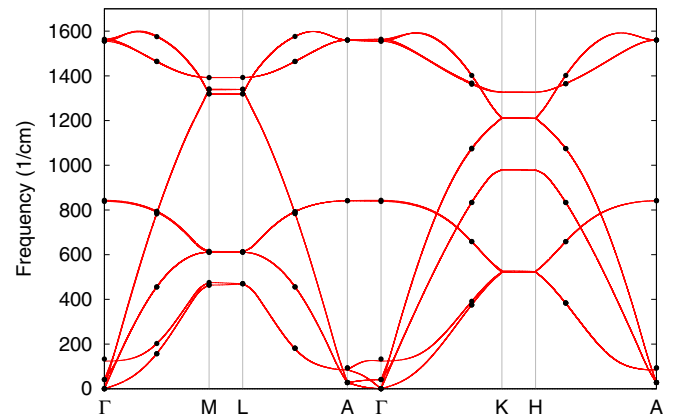


FIG. 1. Phonon dispersion of graphite calculated with the optB86b-vdW functional. Lines show the LNR result and filled circles represent the frequencies calculated by the frozen phonon method.

TABLE I. Elastic constants C_{ij} of graphite (in GPa) calculated by the LNR and FD methods.

	Clamped-ion		Relaxed-ion		Expt. ^a
	LNR	FD	LNR	FD	
C_{11}	1073.8	1071.6	1047.7	1047.2	1060
C_{12}	173.8	173.1	199.9	197.5	180
C_{13}	-3.0	-3.2	-3.0	-3.2	8
C_{33}	38.5	38.1	38.5	38.1	37
C_{44}	5.0	4.9	5.0	4.9	5

^aReference [47].

by the LNR and FD methods, showing the agreement between the two approaches.

To make the comparison rigorous, I recalculate the clamped-ion elastic constants in the following way. In the FD calculations, the plane-wave basis set and the reciprocal vectors to expand the charge density are generated for the unperturbed system and used for the strained systems. The kinetic-energy smearing function is not adopted in both the LNR and FD calculations. These treatments are expected to reduce numerical errors. The values computed by the LNR (FD) method are 1070.36 (1070.38), 172.05 (172.09), -3.50, (-3.50), 38.53, (38.47), and 4.89 (4.85) GPa for C_{11} , C_{12} , C_{13} , C_{33} , and C_{44} , respectively. It can be confirmed that the two methods give very similar values within 0.1 GPa. This agreement supports the validity of the derived formulas and their implementation.

B. MoS₂

Molybdenum disulfide (MoS₂) has attracted much attention for many applications such as dry lubricant [48], nanoelectronic devices [49], and electrocatalyst for the hydrogen evolution reaction [50]. In this section, I apply the LNR method with the optB88b-vdW functional to MoS₂ and compare these results with the GGA-PBE ones. The cutoff energies are set to be 15 and 240 hartrees for the wave function and charge density, respectively. A Γ -centered $12 \times 12 \times 4$ k -point mesh is used for the Brillouin zone integration. In the LNR phonon calculations, the dynamical matrices are calculated on a Γ -centered $6 \times 6 \times 2$ q -point mesh.

The structure of MoS₂ belongs to space group $P6_3/mmc$ (No. 194). The unit cell is composed of two MoS₂ layers in which S atoms form edge-shared triangular prisms and Mo atoms sit on the centers of them. The different layers are weakly bounded by the vdW interaction. In Table III, the crystallographic parameters predicted with the optB88b-vdW and GGA-PBE functionals are listed. The parameters obtained by

 TABLE II. Force-strain coupling constants of graphite (in hartree/bohr) calculated by the LNR and FD methods. The force and strain components are x and xx , respectively.

	LNR	FD
$C(0, 0, 1/4)$	0.2302	0.2301
$C(1/3, 2/3, 1/4)$	-0.2343	-0.2342

 TABLE III. Crystallographic parameters of MoS₂. Space group: $P6_3/mmc$ (No. 194). Lattice constants, a and c (Å). Atom positions: Mo $2c$ ($1/3, 2/3, 1/4$), S $3a$ ($1/3, 2/3, z$). Mo-S bond length d (Å) and Mo-S-Mo bond angle θ (deg.). The results calculated with the optB88b-vdW (vdW) and GGA-PBE (GGA) are shown.

	vdW	GGA	Expt. ^a
a	3.170	3.187	3.161
c	12.443	14.295	12.299
z	0.6239	0.6406	0.625
d	2.410	2.414	2.386
θ	82.22	82.59	82.96

^aReference [51].

optB88b-vdW are in good agreement with the experimental data, whereas GGA-PBE overestimates the lattice constant c by about 16%. Since the in-plane parameters, the Mo-S bond length and Mo-S-Mo bond angle, obtained by GGA-PBE are close to the optB88b-vdW ones, the failure of GGA-PBE is attributed to the lack of the vdW interaction between MoS₂ layers. The electronic structure is predicted to be nonmetallic with both functionals. The optB88b-vdW (GGA-PBE) functional gives an indirect band gap of 0.9 (1.4) eV from Γ to $\Gamma-K$ (K).

Figure 2 depicts the phonon dispersions calculated with the optB88b-vdW and GGA-PBE functionals at each theoretical lattice constants. Both functionals give dispersion curves similar to each other for high-frequency optical modes (>250 cm⁻¹) because of their similar in-plane geometries of the MoS₂ layer. In the low-frequency region, however, GGA-PBE incorrectly shows the soft-mode instabilities around the Γ point. This is probably related to the overestimation of the lattice constant c with GGA-PBE. The soft mode of $29i$ cm⁻¹ at the Γ point has the B_{2g} symmetry, whose eigenvector corresponds to rigid displacements of two MoS₂ layers in opposite directions along the c axis. The optB88b-vdW functional shows no soft-mode instabilities and reproduces well the

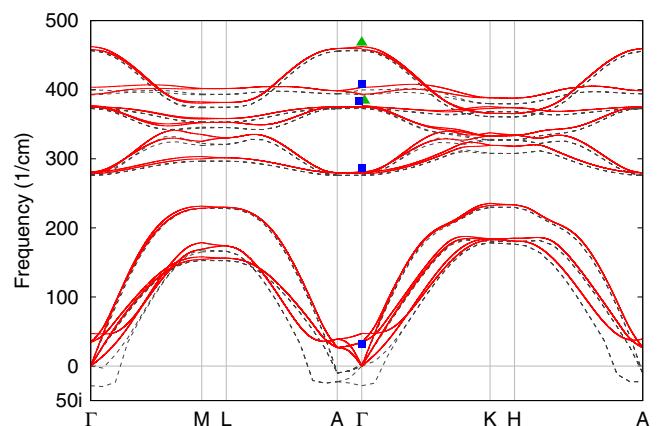

 FIG. 2. Phonon dispersion of MoS₂ calculated with the optB88b-vdW (solid red line) and GGA-PBE (dashed gray line) functionals. Blue squares and green triangles show the experimental data with the Raman [52] and infrared absorption [53] spectroscopies, respectively.

TABLE IV. Elastic constants C_{ij} of MoS₂ (in GPa). The results calculated with the optB88b-vdW (vdW) and GGA-PBE (GGA) functionals are shown.

	Clamped-ion		Relaxed-ion		Expt. ^a	Calc. ^b
	vdW	GGA	vdW	GGA		
C_{11}	266	265	229	228	238	238
C_{12}	81	82	57	57	-54	64
C_{13}	98	99	13	12	23	12
C_{33}	301	301	60	55	52	57
C_{44}	143	143	19	16	19	18

^aReference [54].

^bReference [55].

experimental data observed by the Raman [52] and infrared absorption [53] spectroscopies. Two infrared active modes show small splitting between the transverse- and longitudinal-optical phonons, about 2 cm^{-1} , suggesting that this compound is less ionic. The average values of the Born effective charge tensors, $\frac{1}{3}\text{Tr}[Z^*]$, are -0.85 and 0.43 for Mo and S, respectively. A small positive value for S atoms indicates that they are not anionic. It is expected that in-plane Mo-S bonds are primarily covalent.

The calculated elastic constants are shown in Table IV. To eliminate the soft-mode instabilities for GGA-PBE, the lattice constants are fixed at the experimental values. This treatment is necessary to obtain the relaxed-ion constants. For comparison, the optB88b-vdW calculations are also performed with the experimental lattice constants. Interestingly, GGA-PBE provides the elastic constants quite close to the optB88b-vdW results. A similar match is found for graphite: The clamped-ion constants calculated by GGA-PBE at the experimental lattice constants agree with the optB88b-vdW values within 3 GPa (not shown). The GGA functionals might give a reasonable response to strain if the lattice constants are fixed at the experimental values. Considerable differences between the clamped-ion and relaxed-ion constants are found for C_{13} , C_{33} , and C_{44} . In the clamped-ion case, the in-plane geometry of the MoS₂ layer is uniformly deformed causing large energy cost. Most of this cost is released by the atom relaxation along the c axis due to the weak interaction between MoS₂ layers. The calculated relaxed-ion constants are in reasonable agreement with the experimental data [54], except for C_{12} . The calculated C_{12} is positive while the experimental value is negative. The reason for this discrepancy is uncertain. The positive C_{12} similar to the present result was reported in the previous calculation using the hybrid functional combined with the semiempirical vdW correction [55].

Recently, few-layer MoS₂ samples were fabricated for electronic and optoelectronic applications and Raman spectroscopy was used to investigate the sample thickness [52,56]. Thus, the Raman spectra are predicted for thin-layer MoS₂ samples and compared with the bulk spectrum. Single, double, and triple layers are considered. The thin-layer samples are simulated using a repeating slab model, where the lattice constant a is fixed at the experimental value and c is set to be 25 \AA . The Raman spectra are calculated by assuming the backscattering geometry parallel to the c axis for the

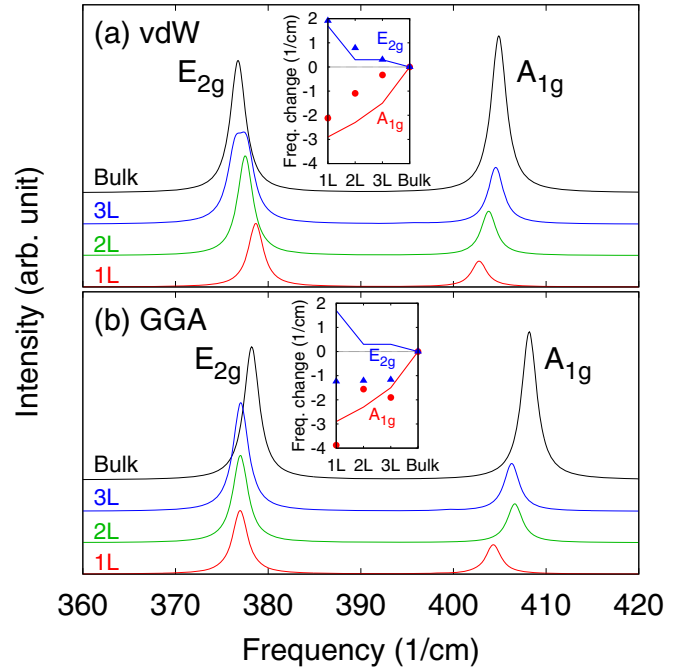


FIG. 3. Raman spectra of thin-layer and bulk MoS₂ calculated with (a) optB88b-vdW and (b) GGA-PBE. The Lorentzian broadening with a width of 1 cm^{-1} is used. The thickness of thin-layer MoS₂ is labeled as 1L: Monolayer, 2L: Bilayer, and 3L: Trilayer. The insets show the frequency changes from the bulk values as a function of the number of layers. The points are the theoretical results and the lines are the experimental results [52].

thin-layer samples. For bulk MoS₂, the average over possible polarization vectors is taken to simulate a polycrystalline sample. The results are shown in Fig. 3. The experimental Raman peaks in bulk MoS₂ are 32 cm^{-1} (E_{2g}), 286 cm^{-1} (E_{1g}), 383 cm^{-1} (E_{2g}), and 408 cm^{-1} (A_{1g}) [52], and the latter two modes are used to identify the sample thickness. The optB88b-vdW functional slightly underestimates the frequencies of these two modes by about 5 cm^{-1} . For thin-layer MoS₂, the calculated Raman peaks show a monotonous upward shift for the E_{2g} mode and a downward shift for the A_{1g} mode with decreasing the number of layers. These features are consistent with the experimental observation [52] though the amount of the downward shift of the A_{1g} mode is somewhat underestimated [see the inset of Fig. 3(a)]. The GGA-PBE functional cannot reproduce these experimentally observed frequency shifts. Though the peaks of the A_{1g} mode tend to shift downward as the number of layers decreases, the peaks of the E_{2g} mode in the thin-layer samples appear on the low-frequency side of the bulk peak and these frequencies are almost constant regardless of the number of layers.

The Raman peak intensity ratios between two modes calculated with the optB88b-vdW functional reasonably agree with the experimental spectra [56]. For trilayer MoS₂, in the frequency range plotted in Fig. 3, an additional Raman active mode is predicted at 396 cm^{-1} due to the symmetry reduction. The origin of this mode is the inactive B_{1u} mode (396 cm^{-1}) in bulk MoS₂. The Raman intensity of the additional mode is, however, two orders of magnitude smaller than those of other Raman active modes. Thus it is hardly observed in Fig. 3(a)

and the two-peak spectral shape is held as found in the experiments. The Raman intensity calculation provides important information, which makes the theoretical predictions of the vibrational frequencies more useful to interpret experimental spectra. In the GGA spectrum for trilayer MoS₂, there is an additional Raman active mode at 399 cm⁻¹, which is also not observed because of its small intensity.

IV. SUMMARY

The linear-response method with the nonlocal van der Waals density functionals has been developed within the ultrasoft pseudopotential scheme. The method deals with three kinds of perturbations: Atomic displacements, uniform electric fields, and strain. The formulas to compute the response with respect to strain are derived for the vdW density functionals as well as for the GGA functionals. The method is applied to weak-coupled layered materials, graphite and MoS₂. For graphite, the comparison between the linear-response and finite-difference calculations shows good agreement, supporting the validity of the derived formulas and their implementation. For MoS₂, it is confirmed that the vdW density functional gives good agreement with experiments,

while the GGA functional fails to reproduce some properties. The present method provides an accurate and efficient way to predict the dynamical, dielectric, and elastic properties for weak-coupled van der Waals systems.

In this paper, the linear-response calculations have been performed using the ultrasoft pseudopotentials. The present GGA formulas to compute the response to strain can be easily implemented for the projector augmented-wave (PAW) method [57]. In the case of the vdW functionals, an approximation has to be introduced as done in the total-energy calculations with the PAW method [43]. Since the interpolation formula for the double spatial integral utilizes the fast Fourier transform, it cannot be applied to the all-electron parts of augmentation functions. The nonlocal vdW correlation energy with PAW, therefore, usually is calculated only on the sum of the pseudo-valence and partial core charge densities. If this approximation is adopted, the present vdW formulas can also be implemented for the PAW method.

ACKNOWLEDGMENT

I thank Y. Kato for valuable discussions about Raman spectroscopy measurements.

-
- [1] E. Wigner, *Phys. Rev.* **46**, 1002 (1934).
 [2] J. P. Perdew and A. Zunger, *Phys. Rev. B* **23**, 5048 (1981).
 [3] J. P. Perdew and Y. Wang, *Phys. Rev. B* **45**, 13244 (1992).
 [4] J. P. Perdew, J. A. Chevary, S. H. Vosko, K. A. Jackson, M. R. Pederson, D. J. Singh, and C. Fiolhais, *Phys. Rev. B* **46**, 6671 (1992).
 [5] J. P. Perdew, K. Burke, and M. Ernzerhof, *Phys. Rev. Lett.* **77**, 3865 (1996).
 [6] Z. Wu and R. E. Cohen, *Phys. Rev. B* **73**, 235116 (2006).
 [7] H. Rydberg, M. Dion, N. Jacobson, E. Schröder, P. Hyldgaard, S. I. Simak, D. C. Langreth, and B. I. Lundqvist, *Phys. Rev. Lett.* **91**, 126402 (2003).
 [8] M. Dion, H. Rydberg, E. Schröder, D. C. Langreth, and B. I. Lundqvist, *Phys. Rev. Lett.* **92**, 246401 (2004).
 [9] K. Lee, E. D. Murray, L. Kong, B. I. Lundqvist, and D. C. Langreth, *Phys. Rev. B* **82**, 081101(R) (2010).
 [10] K. Berland, V. R. Cooper, K. Lee, E. Schröder, T. Thonhauser, P. Hyldgaard, and B. I. Lundqvist, *Rep. Prog. Phys.* **78**, 066501 (2015).
 [11] D. C. Langreth, B. I. Lundqvist, S. D. Chakarova-Käck, V. R. Cooper, M. Dion, P. Hyldgaard, A. Kelkkanen, J. Kleis, L. Kong, S. Li *et al.*, *J. Phys.: Condens. Matter* **21**, 084203 (2009).
 [12] G. Román-Pérez and J. M. Soler, *Phys. Rev. Lett.* **103**, 096102 (2009).
 [13] J. Wu and F. Gygi, *J. Chem. Phys.* **136**, 224107 (2012).
 [14] S. Baroni, P. Giannozzi, and A. Testa, *Phys. Rev. Lett.* **58**, 1861 (1987).
 [15] X. Gonze, *Phys. Rev. B* **55**, 10337 (1997).
 [16] X. Gonze and C. Lee, *Phys. Rev. B* **55**, 10355 (1997).
 [17] S. de Gironcoli, *Phys. Rev. B* **51**, 6773 (1995).
 [18] A. Dal Corso, A. Pasquarello, and A. Baldereschi, *Phys. Rev. B* **56**, R11369(R) (1997).
 [19] S. Y. Savrasov, *Phys. Rev. Lett.* **69**, 2819 (1992).
 [20] C. Audouze, F. Jollet, M. Torrent, and X. Gonze, *Phys. Rev. B* **73**, 235101 (2006).
 [21] S. Baroni, S. de Gironcoli, A. Dal Corso, and P. Giannozzi, *Rev. Mod. Phys.* **73**, 515 (2001).
 [22] N. Ohba, K. Miwa, N. Nagasako, and A. Fukumoto, *Phys. Rev. B* **63**, 115207 (2001).
 [23] K. Miwa, *Phys. Rev. B* **84**, 094304 (2011).
 [24] L. Paulatto, F. Mauri, and M. Lazzeri, *Phys. Rev. B* **87**, 214303 (2013).
 [25] R. Sabatini, E. Küçükbenli, C. H. Pham, and S. de Gironcoli, *Phys. Rev. B* **93**, 235120 (2016).
 [26] D. R. Hamann, X. Wu, K. M. Rabe, and D. Vanderbilt, *Phys. Rev. B* **71**, 035117 (2005).
 [27] A. Martin, M. Torrent, and R. Caracas, *Phys. Rev. B* **99**, 094112 (2019).
 [28] D. Vanderbilt, *Phys. Rev. B* **41**, 7892 (1990).
 [29] K. Miwa, *Phys. Rev. B* **97**, 075143 (2018).
 [30] K. Miwa and R. Asahi, *Phys. Rev. B* **102**, 174313 (2020).
 [31] R. M. Sternheimer, *Phys. Rev.* **96**, 951 (1954).
 [32] X. Gonze, *Phys. Rev. A* **52**, 1096 (1995).
 [33] K. Miwa, T. Sato, M. Matsuo, K. Ikeda, T. Otomo, S. Deledda, B. C. Hauback, G. Li, S. Takagi, and S. Orimo, *J. Phys. Chem. C* **120**, 5926 (2016).
 [34] K. Miwa, *Phys. Rev. B* **103**, 144106 (2021).
 [35] A. Dal Corso, *Phys. Rev. B* **64**, 235118 (2001).
 [36] S. G. Louie, S. Froyen, and M. L. Cohen, *Phys. Rev. B* **26**, 1738 (1982).
 [37] J. A. White and D. M. Bird, *Phys. Rev. B* **50**, 4954 (1994).
 [38] K. Refson, P. R. Tulip, and S. J. Clark, *Phys. Rev. B* **73**, 155114 (2006).
 [39] A. Dal Corso and R. Resta, *Phys. Rev. B* **50**, 4327 (1994).
 [40] L. C. Balbás, J. L. Martins, and J. M. Soler, *Phys. Rev. B* **64**, 165110 (2001).
 [41] O. H. Nielsen and R. M. Martin, *Phys. Rev. Lett.* **50**, 697 (1983).

- [42] X. Wu, D. Vanderbilt, and D. R. Hamann, *Phys. Rev. B* **72**, 035105 (2005).
- [43] J. Klimeš, D. R. Bowler, and A. Michaelides, *Phys. Rev. B* **83**, 195131 (2011).
- [44] M. Bernasconi, G. L. Chiarotti, P. Focher, S. Scandolo, E. Tosatti, and M. Parrinello, *J. Phys. Chem. Solids* **56**, 501 (1995).
- [45] I. Hamada, *Phys. Rev. B* **89**, 121103(R) (2014).
- [46] Y. X. Zhao and I. L. Spain, *Phys. Rev. B* **40**, 993 (1989).
- [47] C. S. G. Cousins and M. I. Heggie, *Phys. Rev. B* **67**, 024109 (2003).
- [48] J. M. Martin, C. Donnet, T. Le Mogne, and T. Epicier, *Phys. Rev. B* **48**, 10583 (1993).
- [49] B. Radisavljevic, M. B. Whitwick, and A. Kis, *ACS Nano* **5**, 9934 (2011).
- [50] D. Voiry, M. Salehi, R. Silva, T. Fujita, M. Chen, T. Asefa, V. B. Shenoy, G. Eda, and M. Chhowalla, *Nano Lett.* **13**, 6222 (2013).
- [51] H. McMurdie, M. Morris, E. Evans, B. Paretzkin, W. Wong-Ng, and C. Hubbard, *Powder Diffr.* **1**, 265 (1986).
- [52] H. Li, Q. Zhang, C. C. R. Yap, B. K. Tay, T. H. T. Edwin, A. Oliver, and D. Baillargeat, *Adv. Funct. Matter.* **22**, 1385 (2012).
- [53] Q.-C. Sun, X. S. Xu, L. I. Vergara, R. Rosentsveig, and J. L. Musfeldt, *Phys. Rev. B* **79**, 205405 (2009).
- [54] J. Feldman, *J. Phys. Chem. Solids* **37**, 1141 (1976).
- [55] H. Peelaers and C. G. V. de Walle, *J. Phys. Chem. C* **118**, 12073 (2014).
- [56] K. Golasa, M. Grzeszczyk, R. Bożek, P. Leszczyński, A. Wyszomolek, M. Potemski, and A. Babiński, *Solid State Commun* **197**, 53 (2014).
- [57] P. E. Blöchl, *Phys. Rev. B* **50**, 17953 (1994).